The Editors

Prof. Dr. Rutger A. van Santen
Schuit Institute of Catalysis
Eindhoven University of Technology
Den Dolech 2
5612 AZ Eindhoven
The Netherlands

Dr. Philippe Sautet
Université de Lyon
Institut de Chimie de Lyon
Laboratoire de Chimie
Ecole Normale Supérieure
de Lyon et CNRS
46 Allée d'Italie
69364 Lyon Cedex 07
France

Library of Congress Card No.: applied for

British Library Cataloguing-in-Publication Data
A catalogue record for this book is available from the British Library.

Bibliographic information published by the Deutsche Nationalbibliothek
The Deutsche Nationalbibliothek lists this publication in the Deutsche Nationalbibliografie; detailed bibliographic data are available on the Internet at (http://dnb.d-nb.de).

Composition Laserwords Private Ltd., Chennai, India
Printing Betz-Druck GmbH, Darmstadt
Bookbinding Litges & Dopf GmbH, Heppenheim

Printed in the Federal Republic of Germany
Printed on acid-free paper

ISBN: 978-3-527-32032-5

14
Adsorption and Diffusion in Porous Systems

Kourosh Malek, Thijs J.H. Vlugt, and Berend Smit

14.1
Introduction

In this chapter, we review adsorption and diffusion processes in some selected porous systems. In particular, we will discuss the transport properties of water in protein crystals (Section 14.2), as well as the adsorption (Section 14.3) and diffusion (Section 14.4) of hydrocarbons in zeolites. We end with a discussion on the simulation of diffusion and reaction in functionalized, amorphous nanoporous catalysts, and membranes in Section 14.5.

14.2
Transport in Protein Crystals: Insights from Molecular Simulations

14.2.1
Introduction

This section provides simulation of transport processes in protein crystals and highlights the importance of protein–solvent and protein–solute interactions. It is of great importance to know whether the catalytic properties of proteins are the same in a crystal and in solution. In their crystalline form, proteins have a highly ordered 3D structure in which the molecules are strongly bound to each other via strong intermolecular interactions. Crosslinked protein crystals (CLPCs) consist of an extensive regular matrix of chiral nanopores, through which ions and solutes travel in and out. CLPCs are especially interesting materials for biotechnological applications to device highly selective biocatalysts, biosensors, and bioseparations. A fundamental understanding of the factors that control the diffusion rate of solutes and solvents in protein crystals is vital for improving and extending the biotechnological applications of such materials. This section focuses on the dynamic properties of water in protein crystals using a lysozyme lattice as a simple model. We also look at distinct features of water and counter-ion diffusion in lysozyme crystals. For a more detailed review of this topic, we refer the reader to Refs. [4, 7–10, 14].

Computational Methods in Catalysis and Materials Science. Edited by Rutger A. van Santen and Philippe Sautet

ISBN: 978-3-527-32032-5

14.2.2
Crosslinked Protein Crystal Technology

Protein crystals are important elements in purification and structure determination of enzymes [1–4]. Such crystals contain pores that range in width from approximately 0.3 nm up to 10 nm, and their porosity is comparable to that of inorganic catalysts and sorbents such as zeolites and silica gel [5]. The complex crystal structure of a protein also contains many functional active sites, where substrates are bound to the protein surface [6]. Recently, CLPCs have been successfully applied as extremely stable biocatalysts and as selective (chiral) separation media. The analysis of water motion in protein crystals is very useful because proteins and other essential biological molecules are in contact through an aqueous medium. In addition to advanced experimental techniques, versatile computational tools are generally needed to correlate the protein's reactivity and the solute's transport with the enzyme crystals' nanoporosity at an atomistic level. MD simulations with explicit representations of molecules and ions should, in principle, provide realistic information about the diffusive motion of water, individual solute molecules, and ions at atomic resolution. Yet, these simulations are practical only at longer time and length scales.

14.2.3
Computational Methodology

A number of computational approaches have been utilized to understand the nanostructure and transport properties of protein crystals. In the following, we dwell a computational approach based on MD simulations to examine molecular motions in orthorhombic and tetragonal lysozyme lattices (LYZO and LYZT, respectively).

Lysozyme consists of 129 amino acids with 1001 nonhydrogen atoms. In a simulation of a single-unit cell at pH = 7, one assumes that the amino acids Glu and Asp are deprotonated, while the Lys, Arg, His residues are protonated. The latter leads to +8 electron charges per protein molecule. The lysozyme crystal structure comes from the Brookhaven Protein Database and serves as a starting point for the simulations. In the case of the orthorhombic crystal (LYZO), there are four protein molecules per unit cell related via crystallographic orthorhombic symmetry ($P2_12_12_1$) with $a = 5.9062$ nm, $b = 6.8451$ nm, and $c = 3.0517$ nm. For the tetragonal lattice of symmetry $P4_32_12$ (LYZT), there are eight protein molecules in a unit cell of size $a = 7.91$ nm, $b = 7.91$ nm, and $c = 3.79$ nm. Thus, for the single-unit cell simulations described here, the LYZO system consists of 5372 protein atoms, 13,576 water molecules, and 32 chloride ions, totaling 46,132 atoms. The LYZT system comprised 10,744 protein atoms, 11,005 water molecules, and 64 chloride ions, totaling 43,823 atoms. Figure 14.1 shows the instantaneous configuration of an atomic model for the fully hydrated LYZO and its crystal structure. We can determine channels and cavities in LYZO by using a procedure explained more fully elsewhere [7–9]. Essentially, we start by

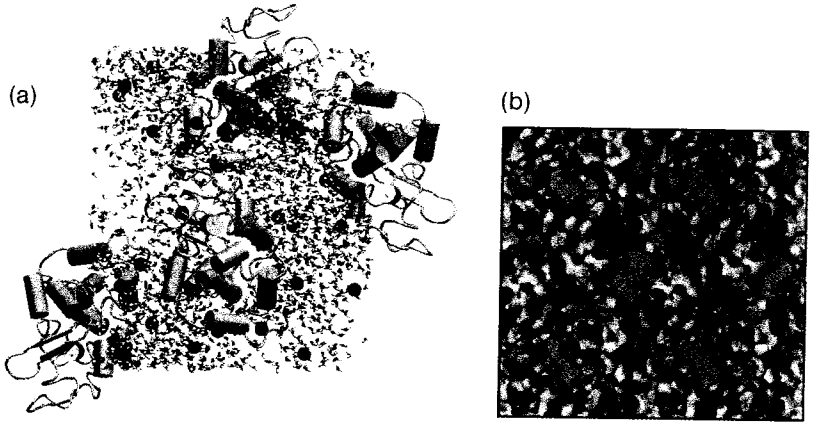

Figure 14.1 All-atom representation of a single-unit cell of orthorhombic lysozyme lattice (LYZO). (a) Blue balls represent chloride ions, and thick ropes represent water molecules. (b) On the lattice surface, hydrophilic and hydrophobic regions are shown in blue and red, respectively. The pore region is in the square [10].

constructing a simulation box, and then we determine a pore radius by calculating the maximum size for diffusing spherical probe to still fit in that pore without overlapping the van der Waals radii of the atoms in the pore wall.

We divide interactions among atoms into nonbonded (between any pair of atoms in a given cut-off radius) and bonded (between atoms connected by chemical bonds). For nonbonded interactions (electrostatic and van der Waals), we assign a partial charge and parameters for repulsion and attraction to each atom. The bonded interaction consists of bond, angle, and dihedral terms, with bond and angle bending given by simple harmonic potentials. The torsional–rotational potential for the dihedral angle is a periodic function with a threefold barrier; a typical effective potential looks like this,

$$
\begin{aligned}
U = & \sum_{\text{bonds}} \frac{k_{b,ij}}{2} \left(r_{ij} - b_{0,ij}\right)^2 + \sum_{\text{angles}} \frac{k_{\theta,ijk}}{2} \left(\theta_{ijk} - \theta_{0,ijk}\right)^2 \\
& + \sum_{\text{dihedrals}} k_\phi \left[1 + \cos\left(n\left(\phi - \phi_0\right)\right)\right] + \\
& + \sum_{i<j} \left[4\varepsilon \left[\left(\frac{\sigma}{r_{ij}}\right)^{12} - \left(\frac{\sigma}{r_{ij}}\right)^{6} \right] + \frac{q_i q_j \operatorname{erfc}(\alpha r_{ij})}{4\pi\varepsilon_0 r_{ij}} \right] \\
& + \frac{1}{2V\varepsilon_0} \sum_{\mathbf{k}\neq\mathbf{0}} \frac{\exp[-k^2/4\alpha^2]}{k^2} \sum_{j=1}^{N} \left| q_j \exp[-i\mathbf{k}\cdot\mathbf{r}_j] \right| ,
\end{aligned}
\tag{14.1}
$$

where r_{ij} is the distance between atoms i and j (or united atoms when CH_n groups are treated as a single interaction site); q_i is the partial charge on atom i; α is

a damping parameter; erfc is the complementary error function; σ and ε are Lennard–Jones parameters; k_b, k_θ, and k_ϕ are force constants for bonds, angles, and dihedrals; n is the dihedral multiplicity, and b_0, θ_0, and ϕ_0 are equilibrium values for the bond lengths, angles, and dihedrals. Here, we model bonds and angles as harmonic oscillators and represent the dihedral term with a cosine expansion. Most importantly, we take into account only the pair interactions; we neglect nonbonded interactions between three or more atoms, and because atoms are represented as point charges, we also neglect electronic polarizability. The last term in Eq. (14.1) corresponds to the Fourier part of the Ewald summation [11]. This term was calculated using a Particle Mesh Ewald (PME) with a grid spacing of 0.12 nm and fourth-order interpolation. All MD simulations described here are performed in a canonical ensemble (*NVT*; given number of particles N, volume V, and temperature T). The Berendsen algorithm controls the temperature by mimicking a weak coupling to an external heat bath at a given temperature T_0 [12]. In the simulations, the weak-coupling algorithm is separately applied for protein, solute, and solvent plus ions with a time constant $\tau = 0.1$ ps and a temperature $T_0 = 300$ K. We use the profile of the root-mean-square deviation (RMSD) from the initial configuration to determine the structure and stability of the protein. Hydrogen atoms are treated as dummy atoms with an increased mass of 4 Da (Dalton number), which can push the integration time step to 5 fs.

The HOLE and CHANNEL algorithms [123, 124] can help us determine cavities and channels in the LYZO and LYZT lattices. Figure 14.2(a) visualizes part of the typical pores along the z-axis in LYZO; the average pore radius in LYZO ($0.68 + 0.02$ nm) is bigger than that in LYZT ($0.52 + 0.02$ nm). Figure 14.2(b) shows the pore radius as a function of pore axis and that each pore has constricted zones inside it. The pore radius in LYZO, for example, slowly decreases from over 0.75 nm to slightly less than 0.61 nm at its narrowest point, whereas in LYZT, it changes from 0.6 nm to 0.45 nm at its narrowest part. An alternative, more indirect, way to look at pore size is to calculate water density as a function of pore

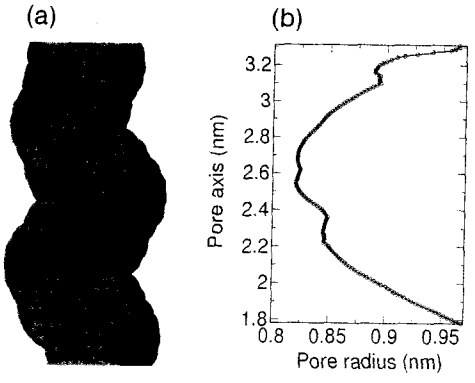

Figure 14.2 (a) A visualized pore along the z-axis in LYZO system. (b) The pore radius profile [10].

axis z. Such calculations yield similar results to those obtained with the HOLE algorithm.

14.2.4 Dynamic Properties of Water Motion

A recent quasielastic neutron-scattering (QENS) study suggested that the water molecules inside the pore region of a triclinic lysozyme crystal could be divided into two populations [13]. The first mainly corresponds to the first hydration shell (surface zone), in which water molecules reorient themselves 5–10 times slower than in the bulk solvent and diffuse by jumps from hydration site to hydration site. The second group (core zone) corresponds to water molecules further away from the protein surface, in an incomplete hydration layer. In protein crystals, this second layer is actually confined *between* hydrated proteins. The self-diffusion coefficient is the most common measure of water mobility because one can use it more readily to compare simulation accuracy to experimental values. For the protein–water interface in a protein nanopore, the dynamic properties of surface water molecules show deviations from those of core zones. QENS studies show that diffusion behavior in the core zone corresponds to a self-diffusion coefficient, reduced approximately 50-fold compared to the diffusivity of free water and almost 10-fold compared with the self-diffusion coefficient of water molecules in the surface zone. Experimental studies also suggest that water mobility is highest close to the protein surface, and, under some crowding conditions, a 2D motion dominates.

Hydration sites are high-density regions in the 3D time-averaged solvent structure in diffraction experiments and in MD simulations of hydrated proteins. The hydration sites are characterized by a combination of an average occupancy and residence time of water molecules. Residence time determines the relaxation time of water molecules in the hydration layer around a given hydration site. The average site occupancy is defined as the average fraction of time that any water molecule occupies the site. We can characterize temporal ordering of the water molecules in a hydration shell of a protein via a population analysis of the hydration sites from which we derive average water residence times. Characterization of hydration sites at the protein surface can also explain the site-to-site jumping mechanism of water motion in a protein nanopore's surface zone. In MD simulations, however, protein hydration sites are defined as local maxima in the water number density map that satisfy certain conditions. They should be no further than 5 Å away from any protein atom and no closer than at least 1 Å. We determine the hydration structure of a lysozyme molecule by computing the water density on the entire surface of the enzyme in solution. By comparing the latter to the experimental hydration structure, we identified a total of 245 and 185 hydration sites around lysozyme molecules in orthorhombic and tetragonal unit cells, respectively. The number of hydration sites can be smaller than that of free proteins in solution because many of the sites in a crystal are buried. In general, the first hydration shell follows the shape of the protein, but in some regions, the hydration sites are

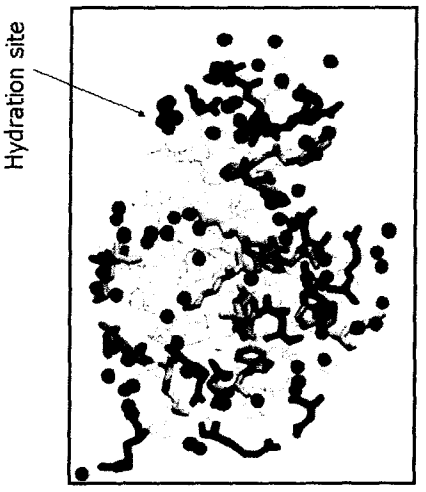

Figure 14.3 Lysozyme hydration sites (red balls) calculated from the solvent-density map data (Lys is yellow, Arg is blue, Asp is purple, Glu is grebe, and Trp is light blue) [10].

clustered. Figure 14.3 shows that charged (Lys, Asp, Glu, and Arg) as well as polar (Trp) residues are located near high-density sites.

The residence times of water molecules on each hydration site are calculated from trajectories of 5 ns. The mean residence time varies for different proteins, but we use a survival probability function $P_{ij}(t, t+\tau)$ to determine the relaxation of water molecules in hydration layers around a protein atom. This probability adopts a value of one if the water molecule labeled j is in the first hydration layer around site i, from time t to time $t+\tau$. The site is considered occupied if a water molecule is found in a spherical volume with radius 1.5 Å (the van der Waals radius of water) centered at this site. The average of the survival probability over all the time configurations and the sum over all water molecules gives the so-called survival function, $P_i(\tau)$. This function is, in fact, the average number of N water molecules belonging to hydration site i that remain on the site after time t. Using this procedure, we calculate the residence time and site occupancy of water molecules in the first hydration layer of lysozyme molecules in LYZO and LYZT systems. Figure 14.4 shows that typical residence time varies between 20 and 700 ps for LYZO and between 10 and 1000 ps for LYZT. For both LYZO and LYZT systems, a Poisson-like residence time distribution is evident. The broad peak on the right-hand side of LYZT's residence-time distributions indicates that there are many hydration sites with long residence time that prolong the life of bound water molecules by up to two orders of magnitude, but such sites are few for LYZO. Residence times of the order of hundreds of picoseconds (strong sites) in a 5 ns simulation are likely due to the visit of a water molecule to a particular site, which is rare over the whole simulation. On average, more than 90% of hydration water molecules have short residence times

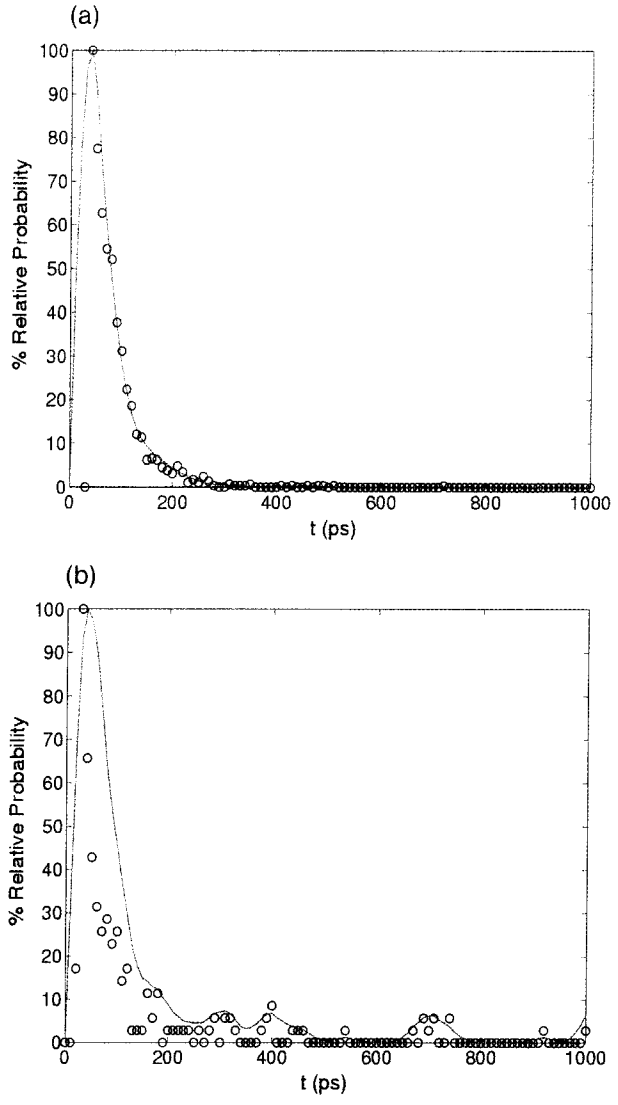

Figure 14.4 Water residence time distributions for (a) LYZO and (b) LYZT systems [10].

(<100 ps), roughly 5% have intermediate residence times (100–500 ps), and the rest have long residence times (>500 ps). The water molecule that enters a site could stay there for a long time period or enter and immediately exit within a short time. Ultimately, the chemical nature of the protein residue close to the hydration shell, the number of hydrogen-binding opportunities, and the protein surface's local geometry (whether a site is buried or exposed) control the residence times.

14.2.5 Water and Ion Diffusion

MD simulations provide lots of information about the static and dynamical pictures found in protein hydration structures. The self-diffusion coefficient D, which is widely used in both spectroscopic experiments and MD simulations, is a suitable parameter for characterizing water's dynamical behavior at the protein–solvent interface. The self-diffusivity D is computed from the slope of the mean-square displacement (MSD) of water molecules by the Einstein relation. The use of the Einstein equation to determine D requires the MSD to be linearly dependent with time. In practice, to determine the water diffusivity, a linear relation between MSD and time must be fulfilled on time scales longer than a few hundred picoseconds. In contrast to the bulk water molecules far from the protein surface (the core zone), water mobility in the protein's vicinity (the surface zone) is restricted. Researchers have also found this in the radial profiles of local diffusion coefficients for a free protein in solution. (In some simulations, translational diffusion in the surface zone is considerably reduced compared to that of bulk water). To analyze water diffusion at both the surface and core zones inside a pore in LYZO and LYZT systems, we consider a selected box of water in the crystal's pore region at a given time and then average the results from five selected boxes in different simulation frames every nanosecond [14]. For each frame of the trajectory, the selected water molecules reorder according to their distance from the water's center of mass and all the other atoms in the protein. An algorithm writes the output trajectories to the surface zone's water trajectory (within 0.3 nm from the protein surface) and that of the core zone (beyond 0.3 nm).

We analyze the MSD versus time for water molecules in the surface and core zones for the two lattices. In all the cases, the log–log behavior is linear with a slope close to one. This slope reaches to one for the bulk water molecules indicating that in fully hydrated pores, the Einstein equation describes the diffusion of water in the core zone. The diffusion coefficient of water molecules in the core zone of LYZT is approximately one half of that in LYZO. For LYZO, the diffusion coefficients in the core (0.21 ± 0.03 nm^2 ns^{-1}) zones are roughly 4% of the diffusion coefficient D_0 of free water ($D_0 = 5.2$ nm^2 ns^{-1} at 310 K). The previous studies show that the rate of solvent diffusion differs in the directions parallel and perpendicular to the surface. In particular, the change in the parallel diffusion rate could be a manifestation of pore-surface irregularity.

To show the differences in the protein–water attachment mechanism for three different ranges of residence times ($\tau < 100$ ps; 100 ps $< \tau <$ 500 ps; and $\tau >$ 500 ps), we collect the number of residues n_r that each diffusing water molecule visited and then computed the probability distribution of n_r for the three time ranges. We collect the number of times water molecules visited a hydration site. For molecules with relatively short residence times (<100 ps), the corresponding probability is higher, meaning that water molecules with longer residence times visit a given site less frequently. For hydration sites near the protein surface, it seems that a water molecule reorients itself much slower than in the core zone.

The molecules in the first hydration shell not only reorient themselves, but they also jump between hydration sites with a broad range of residence time on each site, from 10 ps up to 500 ps; few water molecules with residence times higher than 0.5 ns bound to a protein surface very strongly. We calculate the average jumping length (the average displacement between two successive jumps) for these water molecules in LYZO and LYZT, and found that to be five- and eightfold less, respectively, than that for free water. Water molecules further from the protein surface undergo a long-range translation and are often confined within the pore wall's hydrated proteins. The average MSD of these water molecules has a long-range diffusion coefficient 25- and 40-fold less than D_0 for LYZO and LYZT, respectively. Therefore, such molecules move five times slower than water molecules in the surface zone. Note that water molecules in the second layer act as a water reservoir for the first hydration layer. A mobile and rapidly exchanging hydrogen-bonding network that interacts with protein surface atoms allows for this dynamic behavior. Also note that no part of the solvent in a pore behaves like free water does. Water molecules close to the protein surface show a higher mobility, most likely because of the reduced space available for the solvent at the water–protein interface. For a highly confined system (such as ion channels), the diffusion rate of water is fastest on the surface; conversely, in free protein in water, diffusion is slower close to the protein surface and faster in the bulk. Although a complete understanding is still forthcoming [15], molecular simulations highlight the importance of the water dynamics on transport processes in CLPCs. Despite simplifications, the computer simulations address key issues such as residence time distribution, occupancy, and self-diffusion of water molecules in CLPCs. The essential parameters such as electrostatic interactions should be adjusted for better understanding the principle mechanisms of water and solvent motion in CLPCs. Moreover, a theoretical framework should be developed that can complement and refine simulation approaches.

14.3
Adsorption of Hydrocarbons in Zeolites

14.3.1
Introduction

Zeolites are microporous crystalline materials with pores of about the same size of a small molecule like water or *n*-hexane. The structure of a zeolite consists of covalently bonded TO_4 units, in which the T atom is usually a silicon (Si) or aluminum (Al) atom. To obey charge neutrality, the substitution of a silicon atom by an aluminum atom requires the presence of a nonframework cation (usually Na^+ or K^+) or a proton (H^+). There are approximately 170 different zeolite framework types that have been synthesized [16]. Figure 14.5 shows the pore structure of MFI-type zeolite. Zeolitic materials are widely used as water softener, selective adsorber, and catalyst for hydrocarbon conversions (catalytic cracking and isomerization) [17].

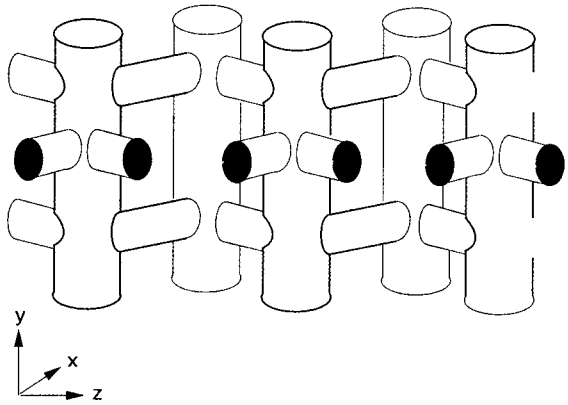

Figure 14.5 Schematic representation of the pore structure of MFI-type zeolite. Straight channels (along the y-axis) are connected by zigzag channels (xz-plane) that cross at the intersections. The all-silica version of MFI-type zeolite is often called silicalite.

As molecular simulations can provide a fundamental understanding of processes and properties at the molecular scale, in the past few years these type of simulations have become an important tool for investigating the adsorption properties of small guest molecules in zeolite hosts. In particular, simulations have been used to study the adsorption of alkanes [18–27], alkenes [28–31], water [32–35], and aromatics [36–42]. For the comprehensive review on this topic, we refer the reader to Ref. [125].

As guest–zeolite interactions are often dominated by the dispersive interactions of oxygen atoms with the guest [43], classical force fields based on Lennard–Jones (LJ) interactions have become very popular in this field of research, especially for alkanes. Intramolecular interactions usually consist of bond stretching, bond bending, and torsion potentials, as well as nonbonded interactions for atoms separated more than three bonds. For adsorption of polar molecules such as benzene and CO_2, as well as for systems with nonframework cations, it is important to take the partial charges on the guest and the zeolite atoms into account; these are usually handled by the Ewald summation [11]. Nonframework cations cannot be neglected as they have a strong effect on adsorption properties, see for example Refs. [44–52]. To enable the use of efficient grid interpolation techniques to compute guest–zeolite interactions [53], the zeolite framework is often kept rigid. Framework flexibility usually does not have a large influence on adsorption properties [54]. However, this can be different when studying transport properties like the diffusion [55–57].

As explained in Chapter 7, the configurational-bias Monte Carlo (CBMC) technique can be used to efficiently compute the thermodynamic properties of guest molecules inside the pores of zeolites [11, 22, 58]. In a typical MC simulation, it is chosen at random with a fixed probability where trial move is performed: translation or rotation of a randomly selected guest molecule, (partial) regrow of

a randomly selected guest molecule using CBMC, insertion or deletion of a guest molecule using CBMC (only for simulations in the grand-canonical ensemble, it is decided at random to insert (50%) of delete (50%) a guest molecule), identity change of a guest molecule (only for mixtures in the grand-canonical ensemble). For more simulation details, we refer the reader to Refs [22, 25].

14.3.2 Obtaining Force-Field Parameters by Fitting Experimental Adsorption Isotherms

Suitable force-field parameters are a key ingredient for computing thermodynamic properties of hydrocarbons in zeolites that agree well with experiments. Dubbeldam *et al.* [25, 26] have shown that reliable interaction parameters can be obtained by fitting simulations to a set of experimental adsorption isotherms (average loading $\langle N \rangle$ as a function of the pressure P or fugacity f). The force-field parameters are especially sensitive to isotherms with *inflection behavior*, e.g., a kink in the adsorption isotherm. While the isotherms of most alkanes for silicalite (all-silica MFI-type framework) show a conventional Langmuir isotherm, i.e.,

$$\frac{\langle N \rangle}{\langle N \rangle_{\max}} = \frac{P}{a + P}, \tag{14.2}$$

isobutane and heptane show an inflection behavior at a loading of approximately four molecules per unit cell of the zeolite (corresponding to approximately 0.7 mol per kg zeolite). For heptane, this is due to the so-called *commensurate freezing* effect [20, 59]. In the case of isobutane, the inflection behavior occurs because of the size and shape of an isobutane molecule relative to the size and shape of the channels and intersection of silicalite [21] (see Figure 14.6). To investigate this inflection, we have plotted the siting of isobutane at a pressure of 0.1 kPa (before the inflection) and 200 kPa (after the inflection) at 308 K and compared this with the siting of butane (see Figure 14.7). The differences are striking. While *n*-butane has approximately an equal probability to be in the straight channel, zigzag channel or intersection, isobutane has a strong preference for the intersection as most space is available there. Let us now compare the siting of isobutane before (low loading, Figure 14.7(b)) and after (high loading, Figure 14.7(c)) the inflection point in the isotherm. Below a loading of four molecules per unit cell, isobutane occupies only the intersections. At a loading of four molecules per unit cell, the intersections are fully occupied and to achieve higher loadings, isobutane must also seek residence in the other channels. This, however, is energetically very demanding and requires a significantly higher driving force (pressure) resulting in the inflection behavior. Only a *single* pair of LJ parameters (ε, σ) is able to correctly describe the experimental adsorption isotherms (see Figure 14.6). Similar inflection behavior is found for other branched alkanes. The inflection behavior of branched alkanes has severe consequences for adsorption isotherms of mixtures of linear and branched alkanes [60–65].

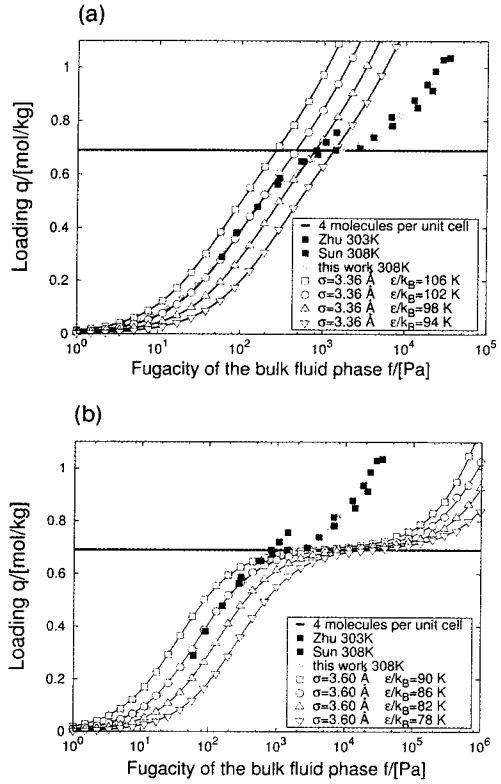

Figure 14.6 Isotherms of isobutane at 308 K in silicalite. The O–CH parameters remain fixed at $\sigma = 3.92$ Å and $\varepsilon/k_B = 40$ K, while ε_{O-CH_3} is examined over a range of reasonable values for two fixed values of σ_{O-CH_3} (a) a rather too small of $\sigma_{O-CH_3} = 3.36$ Å and (b) a too high value of $\sigma_{O-CH_3} = 3.60$ Å. Only a single parameter pair, $\varepsilon_{O-CH_3}/k_B = 93$ K and $\sigma_{O-CH_3} = 3.48$ Å is able to describe the experimental data of Sun *et al.* [66] and Zhu *et al.* [67]. Figure reproduced with kind permission of Ref. [25].

14.3.3 Adsorption of Alkanes at Low Loading

In Table 14.1, we have plotted the Henry coefficient and the heat of adsorption of linear alkanes (with CN carbon atoms) in silicalite. The heat of adsorption ΔH is a linear function of the carbon number, CN. The simulations using the force field of Dubbeldam *et al.* [25] are in excellent agreement with the experiments of Denayer *et al.* [68]. It is important to note that the experiments of Denayer *et al.* have *not* been used to calibrate the force field. In fact, the force field of Dubbeldam *et al.* is transferable to many other all-silica zeolite structures that have not been used to calibrate the force field [25, 27].

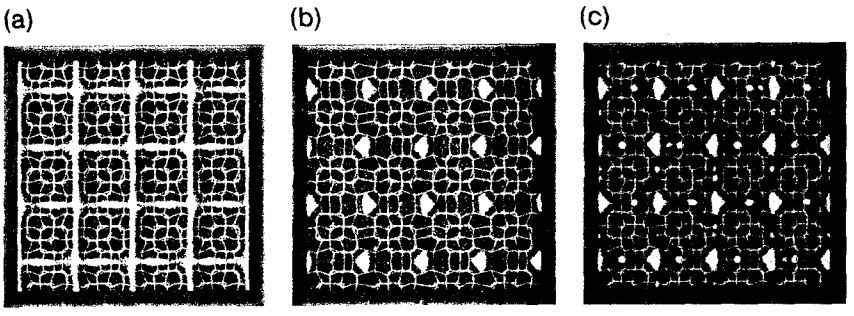

Figure 14.7 Probability distributions of *n*-butane at 0.1 kPa (a), isobutane at 0.1 kPa (b) and isobutane at 200 kPa (c) on silicalite at 300 K. The zigzag channels are from the left to the right and the straight channels are perpendicular to the zigzag channels (projection on the *xy* plane), see also Figure 14.5. These figures were obtained by plotting the centers of mass of the molecules (blue dots) every 200 MC cycles until 10,000 points were collected.

Table 14.1 Comparison of computed low-coverage properties in MFI with the experimental results of Denayer *et al.* [68].[a]

CN	K_H 573 K (mol kg^{-1} Pa^{-1})		K_∞ (mol kg^{-1} Pa^{-1})		$-\Delta H$ (kJ mol^{-1})	
	Simulation	Experiment	Simulation	Experiment	Simulation	Experiment
5	3.04×10^{-6}	2.99×10^{-6}	2.33×10^{-11}	2.64×10^{-11}	56.13	55.7
6	6.10×10^{-6}	5.93×10^{-6}	6.07×10^{-11}	6.07×10^{-11}	65.87	66.0
7	1.23×10^{-5}	1.22×10^{-5}	1.53×10^{-12}	1.29×10^{-12}	75.77	76.7
8	2.43×10^{-5}	2.49×10^{-5}	3.67×10^{-13}	3.25×10^{-13}	85.82	86.6
9	4.61×10^{-5}	4.73×10^{-5}	8.59×10^{-14}	8.41×10^{-14}	95.81	96.1

Relation	Simulation	Experiment
$-\Delta H = \alpha \mathrm{CN} + \beta$	$\alpha = 9.93$	$\alpha = 10.1$
$-\ln(K_\infty) = -A\Delta H + B$	$A = 0.141, B = 16.54$	$A = 0.143, B = 16.4$

[a] Both the Denayer and the simulation Henry coefficients K_H of the linear alkanes have been fitted to $K_H = K_\infty e^{\frac{-\Delta H}{RT}}$ in the temperature range $T = 473$–673 K. Here, K_∞ denotes the pre-exponential Henry coefficient, ΔH the heat of adsorption, and $R = 8.31451$ J mol^{-1}K^{-1} the gas constant (table reproduced with kind permission of Ref. [25]).

14.4 Simulating Loading Dependence of the Diffusion in Zeolites Using Rare-Events Simulations

Most of the rare-event simulations are performed in the limit of infinite dilution. At higher concentration, guest–guest interactions can become important. For example, a molecule can occupy a lattice site and hence prevent another molecule to jump to this site. This effect can be incorporated in a kinetic Monte Carlo simulation. More complicated is the case that the presence of other guest molecules changes

the hopping rate. Techniques have been developed by Tunca and Ford [69, 70] or using an approximate theory by Auerbach and coworkers [71–74] to take into account these effects using a simulation approach.

An alternative approach is to assume a distribution of lattice sites in a zeolite and to obtain the hopping rates from fitting to experimental data or to assume certain values and investigate the effect of changes in the hopping rate. These simulations are particularly useful to obtain insight in the mechanism of diffusion. Applications of these simulations have recently been reviewed by Keil *et al.* [75].

A rigorous extension of transition theory to high loading (dcTST) has been proposed by Dubbeldam and coworkers [76–78]. In this technique one computes the free-energy barrier of a tagged particle. The contribution of the other particles in the systems is included in this free-energy barrier and in the recrossing rate. From this hopping rate one can compute the self-diffusion coefficient directly. This diffusion coefficient corresponds exactly with the one that would be obtained from MD simulations if the assumptions underlying the rare-events simulations hold, that is, once a particle has hopped over a free-energy barrier it remains sufficiently long in the free energy minimum such that it can fully equilibrate before jumping over the next barrier. This technique, however, only provides the self-diffusion coefficient and not the collective or Maxwell–Stefan diffusion coefficient [79].

14.4.1 Diffusion of Hydrocarbons in MFI

At present, many experimental and simulation data have been published on the diffusion of hydrocarbons in zeolites; yet it is difficult to open a text on diffusion in zeolites that does not start with a figure similar to Figure 14.8. This figure demonstrates that depending on the experimental technique diffusion coefficients of linear alkanes in MFI are found that can vary many orders of magnitude. Microscopic techniques like pulse field gradient NMR and quasielastic neutron experiments (QENS) are in reasonably good agreement [80]. The more macroscopic techniques that are based on measuring changes in the weight of the zeolite sample can deviate significantly from the microscopic techniques [81]. Many different possible explanations have been put forward, but we are still lacking a detailed understanding. However, the consensus is that molecular simulations are in reasonable agreement with microscopic techniques [82, 83].

It is interesting to discuss the most simple hydrocarbon, methane, in MFI in more detail. This system has been simulated by many groups [53, 56, 84–99, 99–106]. Figure 14.9 shows the diffusion of methane as a function of loading. The difference between Figures 14.8 and 14.9 is that in the former it is implicitly assumed that diffusion coefficients are independent of the loading. Clearly, this figure indicates a much better agreement of various experimental and simulation results. Essential to obtain this agreement is that in Figure 14.9, for each data point the loading has been carefully estimated for each experimental data point. The figure also shows some experimental data points that show large differences. This maybe caused

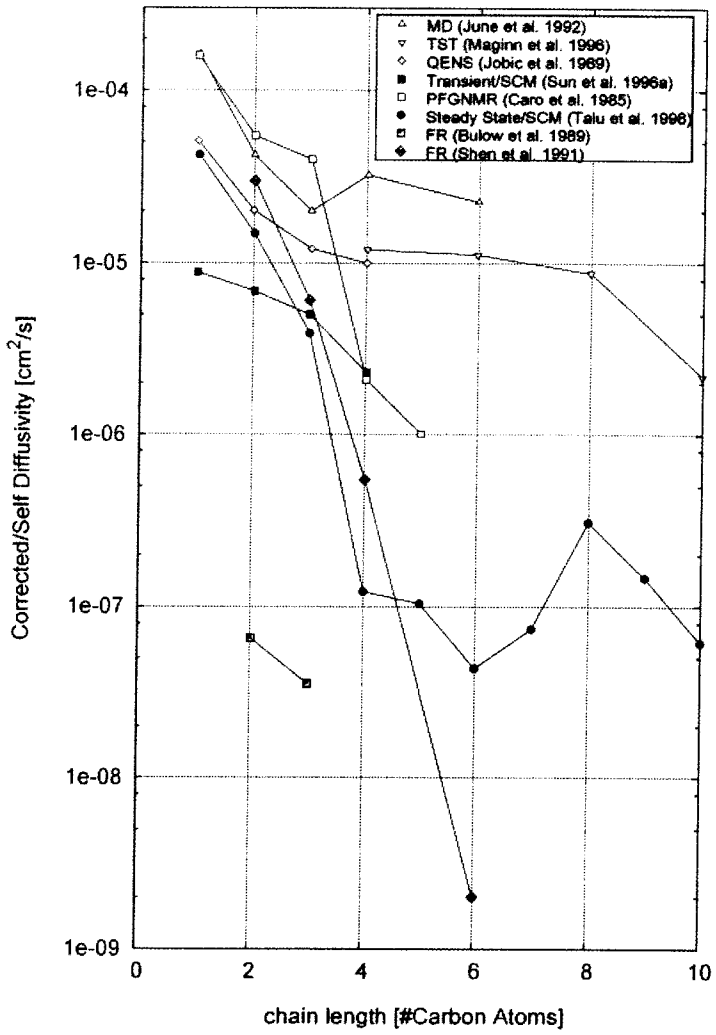

Figure 14.8 Comparison of the experimental and simulated diffusion coefficients of linear alkanes in MFI as a function of chain length.

by a poor estimate of the loading, or that indeed macroscopic techniques also for methane show large deviations.

The interesting phenomena in Figure 14.9 is the peak in the collective diffusion coefficient at 16 molecules per unit cells; careful inspection of the collective diffusion coefficient shows more local maxima (e.g., loadings of 2, 8, or 24 molecules per unit cell). As the accuracy of the simulation results in Figure 14.9 is smaller than the symbol size, these "humps" do not disappear if simulations are extended for a very long time, but this irregular behavior is intrinsic to these systems [107].

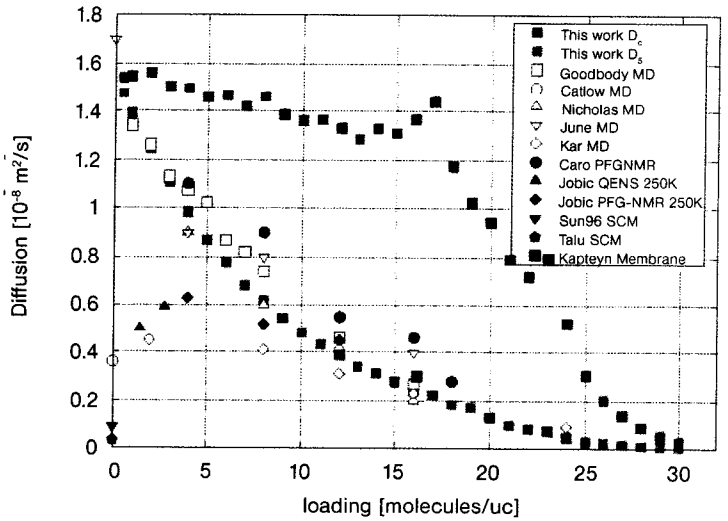

Figure 14.9 Comparison of experimental and simulated diffusion coefficients of methane MFI as a function of loading.

The dcTST transition theory has been used to explain this irregular behavior. This method, however, is used in Ref. [107] in a "wrong way." Instead of using the technique to compute the diffusion coefficient, the technique is used to relate a diffusion coefficient that has been computed with a simple MD simulation to a corresponding free-energy profile. The dcTST method is used to justify that the changes in the free-energy profiles have a one-to-one correspondence to changes in the diffusion coefficient.

Figure 14.10(c) shows that each hump can be associated with a corresponding hump in only one of the three components of the diffusion coefficients. Figure 14.10(d) shows the loading dependence of the free-energy profile of a methane molecule moving along the straight channel (y-direction). At low loading there are three adsorption sites: two in each of the intersections and one in the middle of the channel (the figure shows two minima but only one can be occupied). These adsorption sites are visualized in Figure 14.10(a). If one further increases the loading to the point that all the low-loading adsorption sites are occupied, the system needs to create "space" for the additional molecules. The free-energy profiles show additional adsorption sites at high loading (see Figure 14.10(b)). One can visualize this at low loading the molecules hop on a lattice that suddenly "changes" as the loading is increased. As the number of lattice sites has changed the loading dependence will have a different slope. In addition, at the point the system "switches" from one lattice to the other, the free-energy profile becomes relatively flat and hence causing an increase in the diffusion coefficient. As such changes depend on the details of the channel one can understand that a similar effect occurs in the zigzag channel at a different loading.

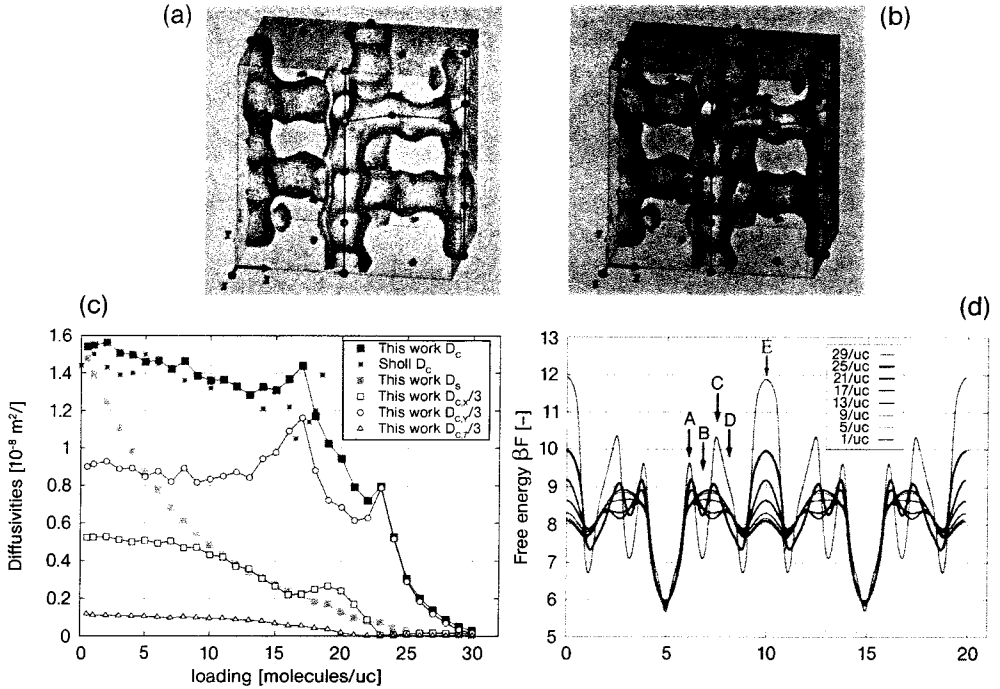

Figure 14.10 Diffusion of methane in MFI: (a) and (b) show the adsorption sites of methane in MFI at low and high loading, respectively, (c) shows the diffusion coefficients in various directions, and (d) the free-energy profile along the straight channel (y-direction) at various loadings. Figure reproduced with kind permission of Refs [107, 108].

The lack of accurate and consistent experimental data, as is suggested in Figure 14.8, makes it very difficult to validate the force field and the assumptions underlying a given model. The fact that in Figure 14.8 all results are plotted in the same figure, irrespective of the loading, illustrates that for a very long time it was assumed that diffusion results in MFI, and many other structures, are independent of the loading. For methane, however, we have shown that a careful analysis of the experimental data illustrates that a part of inconsistencies can be attributed to this assumption. It would be interesting to perform a similar analysis for the other systems.

Beerdsen *et al.* [108, 109] assumed that diffusion can be described by a hopping process from one site to another on a lattice model of the zeolite. For a given molecule, Beerdsen *et al.* computed the free-energy profile of a molecule hopping from one site to another. These free-energy profiles allow to make a classification that helps us understanding the loading dependence. This classification is shown in Figure 14.11. The assumption is that one can model zeolite as ellipsoids. One can make one-dimensional zeolites by placing the cylinders on a line and

connecting them. The circle connecting two cylinders defines the window diameter and depending on the orientation of the cylinders one gets one-dimensional tubes or a zeolite with a more cage-like character. By connecting the cylinders in alternating orientations one can mimic a two- or three-dimensional structure. The corresponding free-energy profiles show that the barrier for diffusion in the case of a tube is very small if the ratio of the window diameter and diameter of the middle part of the ellipsoid is close to one. A very different situation is the cage-like structure in which the windows form a barrier for diffusion, while for the two-dimensional structures the vertically oriented cylinders form entropic traps. The right part of the figure shows some examples of real zeolite structures and the corresponding free-energy profile of methane.

We now consider the effect of increasing the loading; as all ellipsoids are identical for all structures the "second" molecule will be preferentially placed at the same location in the ellipsoid. In fact, to a first approximation, this probability is the highest where the free energy in Figure 14.11 is the lowest. At this point, it is important to mention that the hopping rate and hence the diffusion coefficient is not only determined by the free-energy barrier, but also is the product of this free-energy barrier and the recrossing coefficient. However, for all systems that have been studied this coefficient is a monotonically decreasing function of the loading. We can now envision the following scenarios:

- *Tube-like zeolites.* There is little preference for the additional molecules to be adsorbed. However, as the molecules prefer to be in contact with the walls rather than with another molecule, as a consequence the free-energy profile shifts to higher values but there will be little difference in the shift of the top of the barrier and the bottom. To a first approximation one would expect the free-energy barrier to remain constant and hence the recrossing coefficient causes a decrease in the diffusion coefficient as a function of loading.
- *Cage-like zeolites.* For these zeolites, the preferential adsorption is in the cages. Hence, additional molecules will increase the bottom of the free-energy profile, but not the top. Hence, additional molecules will lower the free-energy barrier and one would expect an increase in the diffusion coefficient.
- *Two- or three-dimensional structures.* Here the adsorption will be both in the horizontal and vertically oriented ellipsoids. In the horizontal ellipsoids they will form an additional barrier and these additional molecules will make the vertically oriented ellipsoids less attractive. As the latter effect will be smaller and the net result is an increase in the free-energy barrier, resulting in a decrease in the diffusion coefficient.

The above free-energy arguments only apply for the self-diffusion coefficient. To understand the collective diffusion coefficient, one has to take into account the lattice topology and other factors that influence the collective behavior. For a more complete review of the diffusion of guest molecules in zeolites, we refer the reader to Refs [110–112].

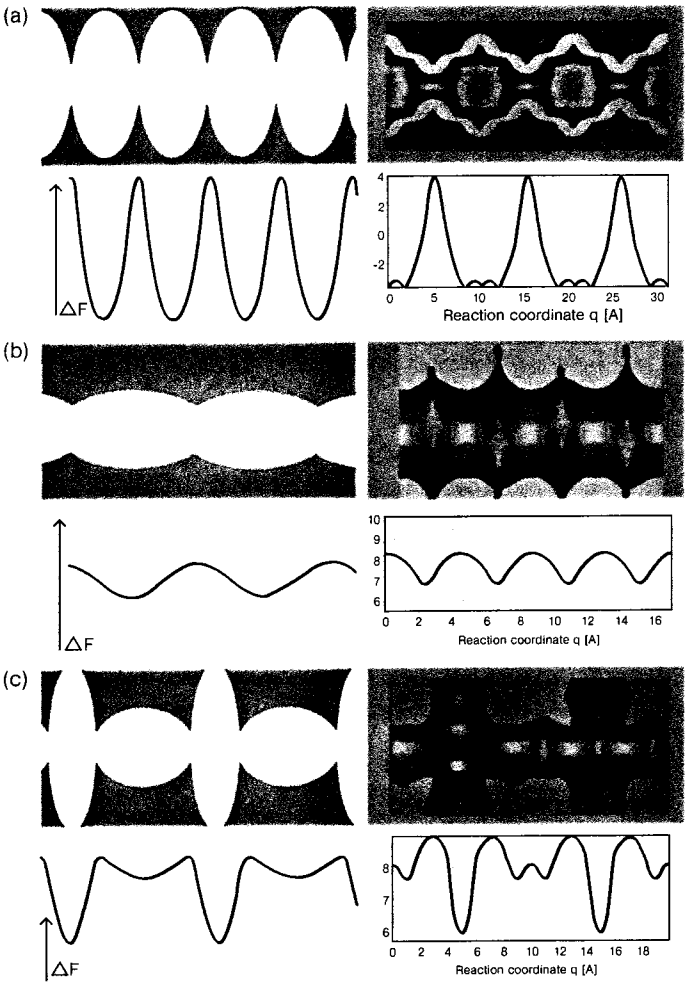

Figure 14.11 Zeolites made out of ellipsoids; the left figures show three ways in which these cylinders can be connected and below the corresponding free-energy profile of a molecule diffusion through these structures. The right figures give an example of real zeolites ((a): SAS, (b): AFI, and (c): MFI) and methane diffusing through them at zero loading. Figure reprinted with kind permission from Ref. [109].

14.5
Simulation of Diffusion and Reaction in Functionalized, Amorphous Nanoporous Catalysts, and Membranes

In a heterogeneous catalyst, reactant molecules diffuse through the pore network, collide with pore walls, and react on active sites on these walls. This implies that the topology of the pore network and the morphology of pores affect the molecular

movement and the accessibility of the active sites. Hence the diffusivities of components and therefore the conversion and product distributions of the reaction depend on the catalyst geometry. On the other hand, porous amorphous catalysts and supports often have a random (fractal) internal surface down to molecular scales [113–116]. This has been confirmed by small-angle X-ray scattering and adsorption studies, and it is a consequence of the specific preparation conditions of these materials, which are often based on a sol–gel synthesis method. Numerous works on the effects of this fractal surface morphology on diffusion and reaction phenomena are performed, from the catalyst fractal pore scale [116], all the way up to the scale of industrial reactors [117, 118]. The attention was initially focused on Knudsen diffusion, since it is expected that it is most influenced by surface roughness, and it is a dominant diffusion mechanism in many gas reactions in mesoporous catalysts. It has been shown how the *gradientless* (self-)diffusion is strongly influenced by surface roughness [116, 119]. A model reaction has also been added to study the effective activity and selectivity as a function of surface roughness [120]. Especially interesting is to find out whether the diffusivities depend on the rates of reactant conversion. This is important for applications, because it shows when it is allowed to use the easier computations based on traditional continuity equations, using (nonfractal) reaction calculations and fractal diffusivities, which were calculated earlier in the absence of reactions. The results have been qualitatively compared to what is known for diffusion in microporous materials. Microporous materials like zeolites are frequently used for separations, adsorption, and catalyst supports. Since these processes are often diffusion limited, it is important to know the molecular diffusivities. The correlation between the chemical heterogeneity and diffusion still remains poorly understood. It is not feasible, if not impossible, to make exact predictions for the effective properties of composite materials with the simple models of morphology. Both continuum and discrete models have been applied to provide and describe the theoretical approaches for estimating the effective properties of random heterogeneous materials. As described above, continuum models represent the classical approach in describing and analyzing transport processes in materials of complex and irregular morphology. Thus, the effective properties of materials are defined as averages of the corresponding microscopic quantities. The shortcoming of discrete models such as random network models, Bethe lattice models, etc., compared to continuum models, is the demand for large computational effort to represent a realistic model to describe the material and simulate its effective properties. It is of course a challenging problem to generate a realization of a heterogeneous material, for which limited microstructure information is available. Based on density functional calculations (DFT and QM/MM), new insights were provided on the importance of electronic and steric effects for epoxidation reaction of *cis*- and *trans*-methylstyren catalyzed by anchored oxo-Mn–salen into MCM-41 channels (see Figure 14.12). All calculations were performed on a catalytic surface with triplet spin state to avoid the complications regard to the Mn-salen spin-crossing [126, 127]. Calculations showed that how immobilization relates to the linker and substrate choice as well as the interplay with the confined channel. Although a *trans*-substrate has a

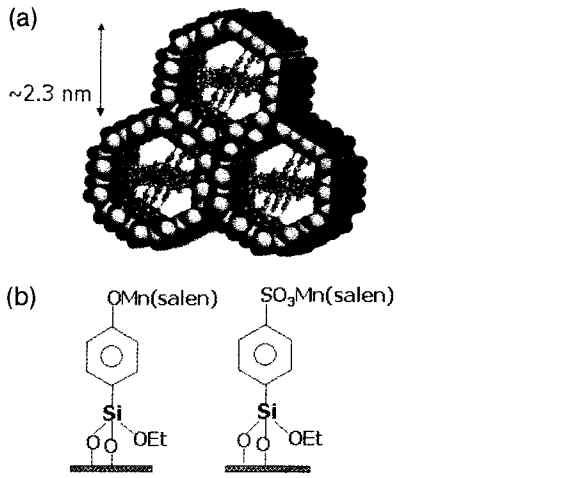

Figure 14.12 (a) Visualized Mn–salen complexes anchored inside a MCM-41 channel using phenoxyl group as the immobilizing linker. (b) The model for the immobilized Mn–salen complexes using different axial linkages [126, 127].

higher level of asymmetric induction to the immobilized Mn–salen complex than that to a homogeneous catalyst, the reaction path is most likely more favorable for the *cis*-substrate. The MCM-41 channel reduces the energy barriers and enhances the enantioselectivity by influencing geometrical distortions of Mn–salen complex.

Novel functionalized nanotube membranes are recently developed and used to efficiently separate a chiral drug from its racemic mixture [121]. Enantiomeric separation in these materials strongly relates to modifier choices and the interplay with the nanopore confinement and substrate–modifier interactions. By means of molecular simulations we propose that the enantioselectivity of such membranes can be improved in a bioinspired way. MD simulations are used to evaluate the capability of a modified silica nanotube for enantiomeric separation of two amino acids, R- and S-2-phenylglycine. This smart nanotube is functionalized as an artificial protein channel in cell membranes. The biomimicry is performed through attaching functional residues (Arg, Glu, Asp) into the nanotube (see Figure 14.13). Simulations indicate that the selective transport of one of the enantiomers (S-) inside the modified channel is strongly affected by the presence of a special electrostatic field inside the channel. The mechanism of enantioselective passage depends on the internal degrees of freedom of the attached residues and interactions of phenylglycine molecules with these residues. The translational–rotational motion of chiral molecules as well as their average dipole orientation is responsible for selective chiral transport inside the nanotube. It is remarkable how configuration of the immobilized residues enhances the enantiomeric separation of the functionalized nanotube. The degree of stereoselectivity in these membranes is as

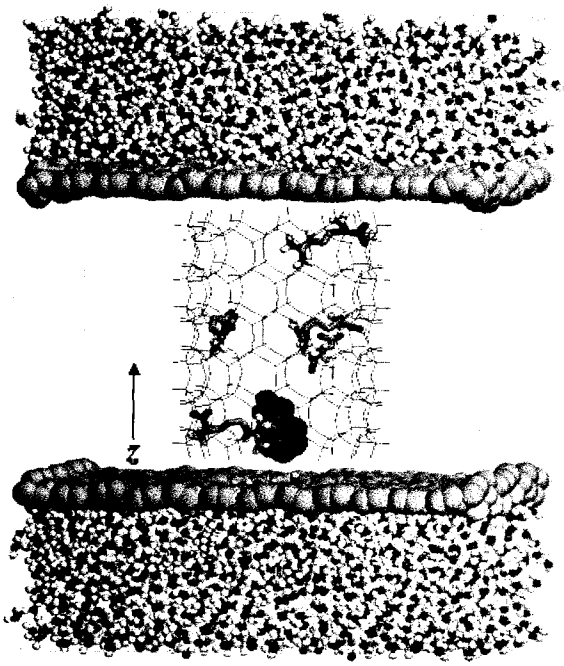

Figure 14.13 The functionalized silica channel is fixed within a slab membrane opening to bulk of water molecules in the two reservoirs at both ends. The phenylglycin molecule is shown in red. Water molecules in the MCM-41 channel are removed for clarity [122].

important as enhancing fluxes across the membrane. We suggest that the enantioselectivity of these membranes can be improved in a nature-inspired way [122]. In order to demonstrate the importance of chiral interactions in atomic scale, within the framework of equilibrium and nonequilibrium MD simulations, we study the complete passage of enantiomers of R- and S-phenylglycine through a modified silica nanotube. The simulations reflect the channel's chiral selectivity for S-isomer. The shape of the electric field, the strength of the force, and translational–rotational motion of chiral molecules are the main reasons for selective chiral transport inside the nanotube. The present results guide future research on biomimic selective chiral membranes, which are able to separate chiral drugs from a mixture.

Acknowledgments

TJHV acknowledges financial support from the Netherlands Organization for Scientific Research (NWO-CW) through a VIDI grant.

References

1 Ohmine, I., Tanaka, H. *Chem. Rev.* **1993**, *95*, 2545.
2 Johnson, L.N., Phillips, D.C. *Nature* **1965**, *206*, 761–763.
3 Vilenchik, L.Z., Griffith, J.P., St. Clair, N., Navia, M.A., Margolin, A.L. *J. Am. Chem. Soc.* **1998**, *120*, 4290–4294.
4 Margolin, A.L., Navia, M.A. *Angew. Chem. (Int. Ed.)* **2001**, *40*, 2204–2222.
5 Morozov, V.N., Kachalova, G.S., Evtodienko, V.U., Lanina, N.F., Morozova, T.Y. *Eur. Biophys. J.* **1995**, *24*, 93–98.
6 Velev, O.D., Kaler, E.W., Lenhoff, A.M. *J. Phys. Chem. B* **2000**, *104*, 9267–9275.
7 Malek, K., Odijk, T., Coppens, M.O. *Nanotechnology* **2005**, *16*, S522.
8 Malek, K., Odijk, T., Coppens, M.O. *Chem. Phys. Chem.* **2004**, *5*, 1596.
9 Malek, K., Coppens, M.O. *J. Phys. Chem. B* **2008**, *112*, 1549.
10 Malek, K. *Comput. Sci. Eng.* **2007**, *9*, 90–95.
11 Frenkel, D., Smit, B., *Understanding Molecular Simulation: from Algorithms to Applications*, 2nd ed., Academic Press; San Diego, **2002**.
12 Berendsen, H.J.C., Postma, J.P.M., van Gunsteren, W.F., DiNola, A., Haak, J.R. *J. Chem. Phys.* **1984**, *81*, 3684–3690.
13 Bon, C., Dianoux, A.J., Ferrand, M., Lehmann, M.S. *Biophys. J.* **2002**, *83*, 1578.
14 Malek, K. *Comput. Sci. Eng.* **2007**, *9*, 70–75.
15 van Hijkoop, J., Dammers, A.J., Malek, K., Coppens, M.O. *J. Chem. Phys.* **2007**, *127*, 085101.
16 Baerlocher, Ch., McCusker, L.B., Olson, D.H., *Atlas of Zeolite Framework Types*, 6th ed., Elsevier; Amsterdam, **2007**.
17 Smit, B., Maesen, T.L.M. *Nature* **2008**, *451*, 671–678.
18 Smit, B., Siepmann, J.I. *Science* **1994**, *264*, 1118–1120.
19 Maginn, E.J., Bell, A.T., Theodorou, D.N. *J. Phys. Chem.* **1995**, *99*, 2057–2079.
20 Smit, B., Maesen, T.L.M. *Natur* *374*, 42–44.
21 Vlugt, T.J.H., Zhu, W., Kapteijn F., Moulijn, J.A., Smit, B., Krish R. *J. Am. Chem. Soc.* **1998**, *120*, 5599–5600.
22 Vlugt, T.J.H., Krishna, R., Smit, B. *J. Phys. Chem. B* **1999**, *103*, 1102–1118.
23 Pascual, P., Ungerer, P., Tavitian, B., Pernot, P., Boutin, A. *Phys. Chem. Chem. Phys.* **2003**, *5*, 3684–3693.
24 Chempath, S., Denayer, J. F. M., De Meyer, K. M. A., Baron, G. V., Snurr, R. Q. *Langmuir* **2004**, *20*, 150–156.
25 Dubbeldam, D., Calero, S., Vlugt, T.J.H., Krishna, R., Maesen, T.L.M., Smit, B. *J. Phys. Chem. B* **2004**, *108*, 12301–12313.
26 Dubbeldam, D., Calero, S., Vlugt, T.J.H., Krishna, R., Maesen, T.L.M., Beerdsen, E., Smit, B. *Phys. Rev. Lett.* **2004**, *93*, 088302.
27 Liu, B., Smit, B. *J. Phys. Chem. B* **2006**, *110*, 20166–20171.
28 Pascual, P., Ungerer, P., Tavitian, B., Boutin, A. *J. Phys. Chem. B* **2004**, *108*, 393–398.
29 Jakobtorweihen, Sven, Hansen, Niels, Keil, Frerich *J. Mol. Phys.* **2005**, *103*, 471–489.
30 Granato, M.A., Vlugt, T.J.H., Rodrigues, A.E. *Ind. Eng. Chem. Res.* **2007**, *46*, 7239–7245.
31 Liu, B., Smit, B., Rey, F., Valencia, S., Calero, S. *J. Phys. Chem. C* **2008**, *112*, 2492–2498.
32 Ramachandran, C. E., Chempath, S., Broadbelt, L. J., Snurr, R. Q. *Microporous Mesoporous Mat.* **2006**, *90*, 293–298.
33 Di Lella, A., Desbiens, N., Boutin, A., Demachy, I., Ungerer, P., Bellat, J. P., Fuchs, A. H. *Phys. Chem. Chem. Phys.* **2006**, *8*, 5396–5406.
34 Desbiens, N., Boutin, A., Demachy, I. *J. Phys. Chem. B* **2005**, *109*, 24071–24076.
35 Desbiens, N., Demachy, I., Fuchs, A.H., Kirsch-Rodeschini, H.,

Soulard, M., Patarin, J. *Angew. Chem. (Int. Ed.)* **2005**, *44*, 5310–5313.
36 Snurr, R.Q., Bell, A.T., Theodorou, D.R. *J. Phys. Chem.* **1993**, *97*, 13742–13752.
37 Lachet, V., Boutin, A., Tavitian, B., Fuchs, A. H. *Faraday Discuss.* **1997**, *106*, 307–323.
38 Lachet, V., Boutin, A., Tavitian, B., Fuchs, A. H. *Langmuir* **1999**, *15*, 8678–8685.
39 Chempath, S., Snurr, R.Q., Low, J.J. *AIChE J.* **2004**, *50*, 463–469.
40 Yue, X.P., Yang, X.N. *Langmuir* **2006**, *22*, 3138–3147.
41 Zeng, Y.P., Ju, S.G., Xing, W.H., Chen, C.L. *Ind. Eng. Chem. Res.* **2007**, *46*, 242–248.
42 Ban, S., van Laak, A., de Jongh, P.E., van der Eerden, J.P.J.M., Vlugt, T.J.H. *J. Phys. Chem. C* **2007**, *111*, 17241–17248.
43 Bezus, A.G., Kiselev, A.V., Lopatkin, A.A., Du, P.Q. *J. Chem. Soc., Faraday Trans. II* **1978**, *74*, 367–379.
44 Buttefey, S., Boutin, A., Fuchs, A. H. *Mol. Simul.* **2002**, *28*, 1049–1062.
45 Beerdsen, E., Smit, B., Calero, S. *J. Phys. Chem. B* **2002**, *106*, 10659–10667.
46 Beerdsen, E., Dubbeldam, D., Smit, B., Vlugt, T.J.H., Calero, S. *J. Phys. Chem. B* **2003**, *107*, 12088–12096.
47 Beauvais, C., Guerrault, X., Coudert, F. X., Boutin, A., Fuchs, A. H. *J. Phys. Chem. B.* **2004**, *108*, 399–404.
48 Calero, S., Dubbeldam, D., Krishna, R., Smit, B., Vlugt, T.J.H., Denayer, J.F., Martens, J. A., Maesen, T.L.M. *J. Am. Chem. Soc.* **2004**, *126*, 11377–11386.
49 García-Pérez, E., Dubbeldam, D., Maesen, T. L. M., Calero, S. *J. Phys. Chem. B* **2006**, *110*, 23968–23976.
50 Liu, B., García-Pérez, E., Dubbeldam, D., Smit, B., Calero, S. *J. Phys. Chem. C* **2007**, *111*, 10419–10426.
51 García-Pérez, E., Dubbeldam, D., Liu, B., Smit, B., Calero, S. *Angew. Chem.-Int. Edit.* **2007**, *46*, 276–278.
52 García-Sánchez, A., García-Pérez, E., Dubbeldam, D., Krishna, R., Calero, S. *Adsorpt. Sci. Technol.* **2007**, *25*, 417–427.
53 June, R.L., Bell, A.T., Theodorou, D.N. *J. Phys. Chem.* **1992**, *96*, 1051–1060.
54 Vlugt, T.J.H., Schenk, M. *J. Phys. Chem. B* **2002**, *106*, 12757–12763.
55 Kopelevich, D.I., Chang, H.C. *J. Chem. Phys.* **2001**, *114*, 3776–3789.
56 Leroy, F., Rousseau, B., Fuchs, A. H. *Phys. Chem. Chem. Phys.* **2004**, *6*, 775–783.
57 Zimmermann, N. E. R., Jakobtorweihen, S., Beerdsen, E., Smit, B., Keil, F. J. *J. Phys. Chem. C* **2007**, *111*, 17370–17381.
58 Smit, B., Siepmann, J.I. *J. Phys. Chem.* **1994**, *98*, 8442–8452.
59 van Well, W.J.M., Wolthuizen, J.P., Smit, B., van Hooff, J.H.C., van Santen, R.A. *Angew. Chem. (Int. Ed.)* **1995**, *34*, 2543–2544.
60 Krishna, R., Smit, B., Vlugt, T.J.H. *J. Phys. Chem. A* **1998**, *102*, 7727–7730.
61 Krishna, R., Vlugt, T.J.H., Smit, B. *Chem. Eng. Sci.* **1999**, *54*, 1751–1757.
62 Schenk, M., Vidal, S.L., Vlugt, T.J.H., Smit, B., Krishna, R. *Langmuir* **2001**, *17*, 1558–1570.
63 Krishna, R., Smit, B., Calero, S. *Chem. Soc. Rev.* **2002**, *31*, 185–194.
64 Krishna, R., Calero, S., Smit, B. *Chem. Eng. J.* **2002**, *88*, 81–94.
65 Smit, B., Krishna, R. *Chem. Eng. Sci.* **2003**, *58*, 557–568.
66 Sun, M.S., Shah, D.B., Xu, H.H., Talu, O. *J. Phys. Chem. B* **1998**, *102*, 1466–1473.
67 Zhu, W., Kapteijn, F., Moulijn, J.A. *Phys. Chem. Chem. Phys.* **2000**, *2*, 1989–1995.
68 Arik, I.C., Denayer, J.F.M., Baron, G.V. *Microporus Mesoporus Mat.* **2003**, *60*, 111–114.
69 Tunca, C., Ford, D. M. *Chem. Eng. Sci.* **2003**, *58*, 3373–3383.
70 Tunca, C., Ford, D.M. *J. Chem. Phys.* **1999**, *111*, 2751–2760.
71 Saravanan, C., Auerbach, S. M. *J. Chem. Phys.* **1997**, *107*, 8120–8131.
72 Saravanan, C., Auerbach, S. M. *J. Chem. Phys.* **1997**, *107*, 8132–8137.
73 Saravanan, C., Jousse, F., Auerbach, S.M. *Phys. Rev. Lett.* **1998**, *80*, 5754–5757.

74 Saravanan, C., Auerbach, S. M. *J. Chem. Phys.* **1999**, *110*, 11000–11011.

75 Keil, F. J., Krishna, R., Coppens, M. O. *Rev. Chem. Eng.* **2000**, *16*, 71–197.

76 Beerdsen, E., Dubbeldam, D., Smit, B. *Phys. Rev. Lett.* **2004**, *93*, 0248301.

77 Dubbeldam, D., Beerdsen, E., Vlugt, T.J.H., Smit, B. *J. Chem. Phys.* **2004**, *122*, 224712.

78 Dubbeldam, D., Beerdsen, E., Calero, S, Smit, B. *J. Phys. Chem. B.* **2006**, *110*, 3164–3172.

79 Krishna, R., Wesselingh, J.A. *Chem. Eng. Sci.* **1997**, *52*, 861–911.

80 Jobic, H., Schmidt, W., Krause, C. B., Karger, J. *Microporous Mesoporous Mat.* **2006**, *90*, 299–306.

81 Karger, J., Ruthven, D. M. *Zeolites* **1989**, *9*, 267–281.

82 Leroy, F., Jobic, H. *Chem. Phys. Lett.* **2005**, *406*, 375–380.

83 Jobic, H., Theodorou, D. N. *J. Phys. Chem. B* **2006**, *110*, 1964–1967.

84 June, R.L., Bell, A.T., Theodorou, D.N. *J. Phys. Chem.* **1990**, *94*, 8232–8240.

85 Demontis, P., Fois, E.S., Suffritti, G.B., Quartieri, S. *J. Phys. Chem.* **1990**, *94*, 4329–4334.

86 Goodbody, S.J., Watanabe, K., MacGowan, D., Walton, J.P.R.B., Quirke, N. *J. Chem. Soc., Faraday Trans.* **1991**, *87*, 1951–1958.

87 Snurr, R.Q., June, R.L., Bell, A.T., Theodorou, D.R. *Mol. Sim.* **1991**, *8*, 73–92.

88 Nowak, A.K., Ouden, C.J.J. den, Pickett, S.D., Smit, B., Cheetham, A.K., Post, M.F.M., Thomas, J.M. *J. Phys. Chem.* **1991**, *95*, 848–854.

89 Hufton, J.R. *J. Phys. Chem.* **1991**, *95*, 8836–8839.

90 Catlow, C. R. A., Freeman, C. M., Vessal, B., Tomlinson, S. M., Leslie, M. *J. Chem. Soc.-Faraday Trans.* **1991**, *87*, 1947.

91 Demontis, P., Suffritti, G.B., Fois, E.S., Quartieri, S. *J. Phys. Chem.* **1992**, *96*, 1482–1490.

92 Demontis, P., Suffritti, G.B., Mura, P. *Chem. Phys. Lett.* **1992**, *191*, 553–560.

93 Kawano, M., Vessal, B., Catlow, C.R.A. *J. Chem. Soc., Chem. Commun.* **1992**, *12*, 879–880.

94 Maginn, E.J., Bell, A.T., Theodorou, D.N. *J. Phys. Chem.* **1993**, *97*, 4173–4181.

95 Nicholas, J.B., Trouw, F.R., Mertz, J.E., Iton, L.E., Hopfinger, A.J. *J. Phys. Chem.* **1993**, *97*, 4149–4163.

96 Smirnov, K.S. *Chem. Phys. Lett.* **1994**, *229*, 250–256.

97 Skoulidas, A. I., Sholl, D. S. *J. Phys. Chem. B* **2001**, *105*, 3151–3154.

98 Skoulidas, A. I., Sholl, D. S. *J. Phys. Chem. B* **2002**, *106*, 5058–5067.

99 Ahunbay, M.G., Elliott, J.R., Talu, O. *J. Phys. Chem. B* **2002**, *106*, 5163–5168.

100 Fritzsche, S., Wolfsberg, M., Haberlandt, R. *Chem. Phys.* **2003**, *289*, 321–333.

101 Bussai, C., Fritzsche, S., Haberlandt, R., Hannongbua, S. *J. Phys. Chem. B* **2004**, *108*, 13347–13352.

102 Bussai, C., Fritzsche, S., Haberlandt, R., Hannongbua, S. *Langmuir* **2005**, *21*, 5847–5851.

103 Hussain, I., Titiloye, J. O. *Microporous Mesoporous Mat.* **2005**, *85*, 143–156.

104 Lopez, F., Perez, R., Ruette, F., Medina, E. *Phys. Rev. E* **2005**, *72*, 061111.

105 Beerdsen, E., Smit, B. *J. Phys. Chem. B* **2006**, *110*, 14529–14530.

106 Krishna, R., van Baten, J.M., García-Pérez, E., Calero, S. *Chem. Phys. Lett.* **2006**, *429*, 219–224.

107 Beerdsen, E., Dubbeldam, D., Smit, B. *Phys. Rev. Lett.* **2005**, *95*, 164505.

108 Beerdsen, E., Dubbeldam, D., Smit, B. *J. Phys. Chem. B* **2006**, *110*, 22754–22772.

109 Beerdsen, E., Dubbeldam, D., Smit, B. *Phys. Rev. Lett.* **2006**, *96*, 044501.

110 Demontis, P., Suffritti, G.B. *Chem. Rev.* **1997**, *97*, 2845–2878.

111 Fuchs, A.H., Cheetham, A.K. *J. Phys. Chem. B* **2001**, *105*, 7375–7383.

112 Dubbeldam, D., Snurr, R.Q. *Mol. Sim.* **2007**, *33*, 305–325.

113 Sahimi, M. *Rev. Mod. Phys.* **1993**, *65*, 1394.

114 Avnir, D., Farin, D., Pfeifer, P. *Nature* **1984**, *308*, 261.

115 Coppens, M.O., in *Fractals in Engineering*, edited by Lévy-Vehel, J., Lutton, E., Tricot, C. Springer; Berlin, **1997**.

116 Malek, K., Coppens, M.O. *Phys. Rev. Lett.* **2001**, *87*, 125505.

117 Sahimi, M., Gavalas, G.R., Tsotsis, T.T. *Chem. Eng. Sci.* **1990**, *45*, 1443.

118 Coppens, M.O. *Colloids Surf. A* **2001**, *187–188*, 257.

119 Coppens, M.O., Froment, G.F. *Fractals* **1995**, *3*, 807.

120 Malek, K., Coppens, M.O. *Chem. Eng. Sci.* **2003**, *58*, 4787.

121 Lee, S.B., Mitchell, D.T., Trofin, L., Nevanen, T.K., Soderlund, H., Martin, C.R. *Science* **2002**, *296*, 2198.

122 Malek, K., van Santen, R.A. *J. Membr. Sci.* **2008**, *311*, 192–199.

123 Smart, O.S. *et al. J. Molecular Graphics* **1996**, *14*, 354–376.

124 Kisljuk, O.S., Kachalova, G.S., Lanina, N.P. *J. Molecular Graphics* **1994**, *12*(4), 305–307.

125 Smit, B., Maesen, T.L.M. *Chem. Rev.* **2008**, *108*(10), 4125–4184.

126 Malek, K., Jansen, A.P.J., Li, C., van Santen, R.A. *J. Catal.* **2007**, *246*, 127–135.

127 Malek, K., Li, C. van Santen, R.A. *J. Mol. Catal. A* **2007**, *271*, 93–104.